AERODYNAMIC CHARACTERISTICS OF TWO ROTARY WING UAV DESIGNS

Henry E. Jones
Oliver D. Wong
Kevin W. Noonan
Deane G. Reis
Brendon D. Malovrh
U.S. Army Aeroflightdynamics Directorate
AMRDEC, U. S. Army Research & Development Command
NASA Langley Research Center
Hampton, Virginia

Abstract

This paper presents the results of an experimental investigation of two rotary-wing UAV designs. The primary goal of the investigation was to provide a set of interactional aerodynamic data for an emerging class of rotorcraft. The present paper provides an overview of the test and an introduction to the test articles, and instrumentation. Sample data in the form of a parametric study of fixed system lift and drag coefficient response to changes in configuration and flight condition for both rotor off and on conditions are presented. The presence of the rotor is seen to greatly affect both the character and magnitude of the response. The affect of scaled stores on body drag is observed to be dependent on body shape.

Introduction

Unmanned Aerial Vehicles (UAV) are remotely piloted or self-piloted aircraft that can carry a variety of payloads and weapons. The wide range of UAV missions require engineering assessments, which must be accomplished by a combination of theoretical, experimental (including wind tunnel and flight test), and computational techniques. Experimental data, in particular, will enhance the ability to support the timely and cost effective development of these and other emerging systems. One of the most critical areas of flight vehicle development is the aerodynamic technologies that deal with the airframe, in particular, the mitigation of adverse aerodynamic forces. These forces include drag, interactional effects such as tail buffet, Reynolds number effects, and the effect of stores on overall aerodynamics. In spite of this need, there appears to be a lack of experimental data to support these developing systems, especially for rotorcraft applications.

For this reason, an experimental investigation of two rotary-wing UAV designs was conducted. The primary goal of the investigation was to provide a set of interactional aerodynamic data for an emerging class of rotorcraft. A supporting goal was to ensure that the geometries employed were readily accessible for easy modeling in available CFD codes. These designs were developed in-house and are based on two generic cross section shapes; a hexagonal shape (Hex Model) and a triangular shape (Tri Model). The designs are 26.5 % scale representatives of an envisioned 3500lb aircraft. The test involved a parametric study of the effect of fuselage shape, rotor presence, wing lift and drag, and store configuration on the fixed and rotating system forces and moments. Pressure data were also taken on both configurations using pressure sensitive paint on the fuselage upper surface. In addition, static pressures were measured on the Hex body using conventional pressure taps. Both configurations were instrumented with a limited set (4) of dynamic pressure taps which were used primarily to calibrate the pressure sensitive paint measurements. Because of the large body of data taken, a complete discussion of the entire test is beyond the scope of a single paper. The present paper is intended to provide an overview of the test and an introduction to the test articles, and instrumentation. Sample data in the form of a parametric study of fixed system lift and drag coefficient response to changes in configuration and flight condition are also presented.

Symbols and Abbreviations

A reference area (27.57), ft^2
c wing chord, ft.
C_D drag coefficient (D/qA)
C_L lift coefficient (L/qA)

D	drag, lb
q	dynamic pressure, $(1/2)\rho V^2$, lb/ft^2
S	surface wetted area, ft^2
V	free stream velocity, ft/sec
α	Angle of attack, deg
β	Angle of sideslip, deg
α_{wing}	Wing angle of attack, deg
ρ	Density of air, slugs/ft^3

Abbreviations

Hex	hexagonal-shaped body
Tri	triangular-shaped body
ESP	electronically scanned pressures
IRTS	isolated rotor test system
KTAS	knots, true air speed
L	lift, lb
LVDT	linear variable differential transformer
MPA	model preparation area
PSP	pressure sensitive paint

Apparatus and Models

The 14X22 Tunnel

The Langley 14 -by 22-Foot Subsonic Tunnel is an atmospheric, closed return tunnel with a test section 14.5-ft high, 21.75-ft wide, and 50-ft long which can reach a velocity of 348 ft/sec with a dynamic pressure of 144 psf (ref 1). The Reynolds number per foot ranges from 0 to 2.2 x10^6 The flow in the closed test section configuration is relatively uniform with a velocity fluctuation of 0.1 percent or less. Test section airflow is produced by a 40-ft diameter, 9-bladed fan. The tunnel has a set of flow control vanes to maintain close control of the speed for low-speed testing. Model force and moment measurements are typically made with 6-component strain-gage balances.

For the present effort, the Isolated Rotor Test System (IRTS) was used to power the rotor. The IRTS consists of a drive motor, balance, and controls for a single rotor. The components are stacked in a linear fashion to provide minimal obstruction to the flow into and out of the rotor disk. A sketch of the IRTS and the model set-up is presented in figure 1. The IRTS is mounted to the non-flow side of the test. section ceiling. The base supports an arc sector to vary the angle of attack of the entire drive system (including the rotor shaft) while maintaining the center of the rotor near the centerline of the test section. A 50 hp electric motor is attached to the arc sector. Power from the motor is transmitted to the

drive shaft by way of two drive belts. A 36 channel slip ring is installed at the base of the shaft to transfer electrical signals from the rotating to the non-rotating system. The hollow drive shaft is supported within a stepped cylinder that forms the external surface of the IRTS. The drive shaft passes through the rotor balance. Electric actuators control a swash plate for rotor collective and cyclic pitch. The end of the drive shaft is designed to accept hubs from the 2-meter rotor test system (reference 2). For this test a similar four-blade, fully articulated hub was used.

Fuselage Models

One of the primary goals of the present effort is to provide a data set which can be used in CFD code validation and calibration. Developing a geometric model of a configuration (i.e. a grid) is the most important first step in any CFD analysis. The fuselage model design process used in the present case was developed in order to insure that each of the basic fuselage shapes were geometrically simple, generic and, most importantly, analytically or numerically defined. Using analytically or numerically defined shapes insures that each basic geometry is readily accessible and hence, easy to grid. Employing generic shapes ensures that the data set is unrestricted and, hence available to a broad number of CFD code developers.

The model configurations chosen belong to a family of nine shapes which are designed based on three cross sections (triangle, hexagonal, and oval) and three longitudinal shape functions (symmetric, convex, and conventional). Each configuration begins as a uniform "cylinder" with a specified cross section. This cylinder is then modified by a shape function to produce the final design. The current models use the conventional shape function which yields the familiar main-body / tail boom layout. Figure 2 presents a pictorial representation of this process. In order to provide a basis of comparison, both models have the same body length, (72 in.) and internal volume (5 ft^3) but differ in surface area. Body length was dictated by physical limitations of available test articles such as the rotor system which is ~ 70 inches in diameter. Internal volume was selected based on a compromise of geometric criteria. Two of the nine fuselage model configurations were selected to be tested; a hexagonal shape (Hex Model, fig 3.) and a triangular shape (Tri Model, fig 4.).

Wing Model

A wing was designed along with these configurations in order to explore the effects of wing lift on

configuration aerodynamics and to provide mount points for rockets. As with the fuselage shapes, the wing was designed to be a simple geometric shape in order to insure ease of modeling. The wing layout was developed by following the description presented by Stepniewski (ref. 3) and using the Apache wing geometry as a guide. The resulting wing layout is a simple linearly tapered shape, employing a NACA 23012 airfoil, and no twist. The wing span is 48.4 in. The root chord is 6.55 in and the tip chord is 4.7 in yielding a taper ratio of 0.717. The wing aspect ratio is 4.3 and overall wing area is 271.8 in^2. Wing area includes the projected area covered by the fuselage. Because of the difference in body width, the exposed wing planform area for the Tri model is ~ 185 in^2 and for the Hex model it is ~ 105 in^2 . The wing was capable of attaching to the body at 0, 3, and 6 degrees relative to the fuselage waterline.

Rotor Model

The rotor used for this test is a representative modern rotor design with a radius of 35.30 in., a nonlinear twist, and a set of modern airfoils. The flapping and lag hinges are coincident at the 2.00 in. radial station. The rotor blades used in this test have a tapered plan-form with a chord of 2.25 inches. The root cutout is about 17 percent of the radius. Further details of the rotor are listed in table 1, which is taken from reference 4. Note that the radius of the hub used in the current effort is 0.25 in. shorter than the one used in reference 4. For the current effort the rotor lift coefficient was set to 0.006 for the entire test.

Configuration Stores and Pylon

Two store configurations were modeled during the current effort. The first was a gun-pod arrangement which is a scaled version of the gun-pod model used in reference 4. The second store configuration was a scaled set of 2 representative rockets which could be attached either together (one port, one starboard) or separately to either outboard wing station.   These stores are shown (attached to the configurations) in both figures 2 and 3. These stores were added to the model in order to provide realistic interference effects on the basic geometries. The stores were also scaled to 26.5% size based on an envisioned 3500lb aircraft. In addition to these stores, the Hex model had an oval shaped pylon which can be seen in figure 2; the Tri model has no pylon.

Instrumentation

Fuselage forces and moments were measured using a conventional six-component strain gage balance. Rotor forces and moments were measured with a five-component strain gauge balance installed in the IRTS. The rotor balance measured the force in each of the three coordinate directions and the pitching and rolling moments referenced about the center of the rotor hub. Rotor torque was measured with two redundant strain gauge bridges on the rotor shaft. Rotor shaft angle was measured using an accelerometer with an accuracy ±0.01°. Actuator extension for the rotor controls was measured using a redundant system of linear variable displacement transducers (LVDTs) and encoders. These outputs were resolved into rotor collective pitch, longitudinal cyclic pitch, and lateral cyclic pitch. Assumed accuracies of the control positions are ±0.5°, based on the hysteresis of the calibrations at the maximum angles (worst case). Hall effect devices were installed on the flapping and lagging hinges to measure the motion of the reference blade. Rotor rotational speed and reference blade azimuthal position were measured using optical encoders. For the 0° azimuthal position, the reference blade was located over the tail. Balance sensitivities and uncertainty are presented in table 2.

Test

Tables 3 and 4 summarize the test matrix.   The test matrix was principally a study of the effect of a systematic variation of configurations and flight conditions on the fixed system aerodynamic forces. Flight conditions were varied using a set of four sweeps as displayed in table 3.   The intent of the trim sweep was to capture representative forces on the configuration in trimmed flight. Trimmed forward flight is typically characterized by a decrease in body angle-of-attack which is necessitated by the need to trim the drag moment of the fuselage which increases with speed. The trim sweep angle-of-attack conditions were based on computations made using the CAMRAD II comprehensive rotorcraft code (reference 5). The CAMRAD II analysis was based on a model of the OH-6 which is representative of the class of the envisioned 3500lb aircraft. Alpha sweeps are intended to capture the basic lift and drag polar of the particular configuration at a representative speed, 100 knots in this case. Alpha variations ranged from -9 to 0 deg. in 3 deg increments. The IRTS rotor shaft was pitched with changes in fuselage α so that the rotor shaft was kept perpendicular to the body

waterline. As with Alpha sweeps, Beta sweeps are intended to capture the basic lift and drag polar of the configuration but in sideward flight. Beta variations ranged from -16 to + 16 degrees in 2 deg increments. Speed sweeps capture the effect of velocity on the body forces. Speeds of 40 to 160 knots in increments of 20 knots were employed to achieve this. Aircraft speed is believed to have a significant effect on the wake skew angle (ref. 4) and hence on body forces. Within the context of these basic sweeps table 4 presents the configuration variations chosen for the test. The dominant configuration changes are body shape and the presence of the rotor. Variations of the wing and rocket configurations were also included in the test.

Discussion of Results

Presentation of the complete data set is beyond the scope of this paper, however a representative selection of data from the test is included in figures 5 through 16. The data are presented in graphic format with a typical graph presenting the variation of the independent variable for both body configurations and for rotor on and rotor off conditions. The variations are presented in sequence with the basic configuration (body + gun-pod) first. The effects of adding the wing (at $\alpha_{wing} = 0°$) are presented next, followed by the effect of adding both rockets. Figures 5 through 10 present the effect on drag coefficient of variations in configuration and test condition, while figures 11 through 16 present the effect on lift coefficient.

Drag Coefficient Variations

Figure 5 presents the variation of basic configuration drag coefficient vs. speed with and without the rotor. Two major effects are apparent from the figure. The first is, for the configurations without the rotor, a gradual drop in drag coefficient with increasing speed occurs representing about an average 11.5% reduction over the speed range tested. This is most probably a Reynolds number effect. The second significant effect is the impact of adding the rotor on the response of both configurations. The rotor downwash significantly increases the drag coefficient for both configurations. The Tri model has an average 22.4% drag rise, while the Hex model has an average 46% increase over the measured speed range. Figure 6 presents the same comparison as figure 5 but with the addition of the wing to the basic

configuration. The wing has little effect on the basic response outlined above except to raise the level of drag for both configurations. Tri model drag coefficient is increased by an average 5.5% with the addition of the wing and no rotor, while the Hex model drag coefficient increases 6.7%. Addition of the rotor adds an average of another 16.7% to the Tri model drag coefficient and another 43.8% to that of the Hex model. Figure 7 presents the drag coefficient response of both the configurations with both wing and rockets mounted. Adding the rockets to the wing (with no rotor present) increases the drag coefficient of both the Tri and Hex models. Addition of the rotor further increases the Tri and Hex model drag coefficients. In order to highlight the effect that the rockets have on the drag response of the two configurations, figure 8 presents a comparison of the variation of drag coefficient with speed for both configurations with and without the rockets mounted on the wing and no rotor (e.g. a rocket only delta). This figure is intended to present an isolated view of the effect that the rockets have on the drag response of the two configurations. The figure shows that the Hex model experiences approximately twice the increase in drag coefficient than does the Tri model with the addition of the rockets. Adding the rockets to the wing (with no rotor present) increases the drag coefficient of the Tri model by 6.1%. The Hex model drag coefficient increases by 13.2%. Addition of the rotor (see figure 7) further increases the Tri model drag coefficient by 18.2 % and it increases the Hex model drag coefficient by an average of 36.2%.

Figure 9 presents the response of the drag coefficient to a variation of angle-of-attack at 100 knots speed and a zero yaw angle for both configurations with and without the rotor. The basic response of both configurations, with no rotor, is the familiar parabolic drag polar. The average difference between the two configurations with no rotor present is 5.9%. Addition of the rotor significantly increases the drag coefficient of both configurations and also increases the separation between the Tri and Hex configurations to about 22.8%

Figure 10 presents the change in drag coefficient of both of the configurations to a variation in yaw angle at 100 knots speed and zero degrees angle-of-attack. For the rotor off configuration, the Hex model drag coefficient is 10.3% higher than the Tri model configuration at $\beta=0°$. As the yaw angle increases, the drag coefficient of the Tri model increases faster than that of the Hex model leading to a cross over at about 11 deg. The addition of the rotor raises the level of drag coefficient for both configurations and increases the difference between them. The Hex

model now has a 27.3% higher drag coefficient, at $\beta=0°$. The rate of increase in drag coefficient with yaw angle, however, is still higher for the Tri model and the two curves cross over again at about 13 deg.

An additional feature of the data in figure 10 is the asymmetry of the curves. Both the Tri and Hex models have higher drag coefficients for positive yaw angles. In addition, the rate of increase of drag coefficient is different for positive and negative yaw angles particularly with the rotor present.

Lift Coefficient Variations

Figure 11 presents the variation of basic configuration lift coefficient with speed with and without the rotor. For the rotor-off case, there is little variation of lift coefficient with speed for either configuration. The Hex model lift coefficient is essentially zero for the whole speed range. The Tri model lift coefficient is approximately -0.0060 for most of the range. Both configurations experience a slight increase in lift coefficient at high speed which may be a Reynolds number effect.

 Introduction of the rotor dramatically changes the lift curves. The impressed downwash from the rotor produces a download on both configurations which greatly reduces the lift coefficient. This download is significantly altered by speed with the largest effect at low speed and the effect tapering off as speed increases. At 60 knots, the Tri model experiences a reduction in lift coefficient of -0.0325, while at 120 knots, the reduction is -0.0085. The Hex model lift coefficient is reduced by -0.0292, at 60 knots and -0.0082 at 120 knots.

Figure 12 presents the same comparison as figure 11 but the wing has been added ($\alpha_{wing}=0°$) to the basic configuration. For the rotor off configuration, the effect of the wing on the Tri model is to add an average increase in lift coefficient of 0.0047 over the speed range. The lift coefficient increase on the Hex model is an average of .0071.

The rotor has the same overall effect on both the winged configurations as it had on the basic configurations but the magnitudes of the changes are larger. At 60 knots, the Tri model lift coefficient is reduced by -0.0518, while at 140 knots the reduction in lift coefficient is -0.0137.   The Hex model lift coefficient is reduced by -0.0543 at 60 knots and by -0.0170 at 140 knots.

Figure 13 presents the same comparison as figure 12 but both the rockets have been added. For the rotor-off configuration, the effect of the rockets on the Tri model is to add an average increase in lift coefficient of 0.0012 over the speed range. The measured lift coefficient change on the Hex model is very small and within the accuracy of the balance.

The rotor has the same overall effect on both the wing plus rocket configurations as it had on the basic configuration plus wing. At 60 knots, the Tri model lift coefficient is reduced by -0.0519, while at 140 knots the reduction in lift coefficient is -0.0139. The Hex model lift coefficient is reduced by -0.0528 at 60 knots and by -0.0164 at 140 knots. The measured changes in lift coefficient between the rocket off and on cases (figures 12 and 13) are all very small and within the accuracy of the balance.

Figure 14 isolates the effect of the wing on lift coefficient variation with alpha for the basic configuration without the rotor present.   For the wing off case, lift coefficient increases with increasing alpha with the difference in lift coefficient between the two configurations being 0.0109 at $\alpha=-9°$ and decreasing to 0.0049 at $\alpha=0°$. Adding the wing increases the magnitude of the lift coefficient for both configurations with the Tri model lift coefficient changing by -0.026 at $\alpha=-9°$ and by 0.0047 at $\alpha=0°$. Note that the wing airfoil section is cambered and hence the lift coefficient will not be zero at $\alpha=0°$.

Figure 15 presents the variation of lift coefficient with angle-of-attack for both configurations with the wing and rockets present and with and without the rotor. The variation in lift coefficient with alpha is the familiar lift curve slope in that lift increases with increasing alpha. At $\alpha=-9°$ with no rotor, the difference in lift coefficient between the two configurations is -0.0028. This difference increases to -0.0070 at $\alpha=0°$. The addition of the rotor shifts the curves downward by about the same amount (-0.0225) at $\alpha=-9°$ and $\alpha=0°$. In addition, the presence of the rotor reduces the difference between the configurations to a small value over the range of angles tested.

Figure 16 presents the change in lift coefficient of both of the configurations to a variation in yaw angle at 100 knots speed and zero degrees angle-of-attack. For the rotor off configuration, the Tri model lift coefficient at $\beta=0°$ is 0.0008 and the Hex model lift coefficient is 0.0080. Lift coefficient increases with yaw angle for both configurations, although more so

for the Hex. Both of the configurations are asymmetric about β=0°, but this effect is more pronounced for the Hex model. The addition of the rotor shifts both configuration lift coefficient curves down. At β=0° the Tri model lift coefficient is decreased by -0.0215 while the Hex model lift coefficient is reduced by -0.0250.

Conclusion

A wind-tunnel test on two rotary-wing UAV designs has been completed. Force and moments data for both the fuselage and rotor have been recorded under a variety of flight conditions. A systematic variation of the model configurations was studied producing a large set of data encompassing variations in both flight condition and geometry. The following observations can be made based on the data presented herein:

1. The rotor has a significant affect on body forces.
2. The affect of scaled stores on body drag is dependent on body shape.
3. Asymmetric effects are observed for yaw excursions for body lift and drag.
4. Reynolds Number effects are likely and were observed for the scaled body shapes tested.

References

1. Gentry, G. L.; Quinto, P. F.; Gatlin, G. M.; and Applin, Z. T.: *The Langley 14- by 22-Foot Subsonic Tunnel: Description, Flow Characteristics, And Guide For Users*. NASATP 3008, 1990.

2. Phelps, A. E.; and, Berry, J. D.: *Description of the Army's 2-Meter Rotor Test System*. NASA TM-87762, AVSCOM TM-86-B-4, 1987.

3. Stepniewski, W. Z.; Keys, C. N. : Rotary-Wing Aerodynamics, Dover Publications, Inc., New York, 1984.

4. Gorton S.A., Berry J.D., Hodges W.T., and Reis D.G.: *Flow Environment Study Near the Empennage of a 15-Percent Scale Helicopter Model*, NASA/TP-2000-210085

5. Johnson, Wayne "*Technology Drivers in the Development of CAMRAD II*," by Wayne Johnson.

Tables

Table1. Description of rotor.

Airfoil section		Number of blades	4
23.7-percent radius VR-12		Pitch axis, percent of chord	25
84.6-percent radius VR-12		Radius, in.	35.30
91.8-percent radius SSC-A09		Solidity, thrust-weighted	0.0787
100-percent radius SSC-A09		Tip sweep angle (of 1/4 chord), deg	30
Chord, in.		Tip sweep begins, in.	31.45
23.7-percent radius 2.25		Twist, deg	
84.6-percent radius 2.25		0-percent radius	0
91.8-percent radius 2.25		23.7-percent radius	0
100-percent radius 1.35		74.3-percent radius	-6.6
Cutout, in. 8.2		84.6-percent radius	-7.6
Flapping hinge offset, in. 2.0		91.8-percent radius	-9.5
Lag hinge offset, in. 2.0		100-percent radius	-9.5

Table 2. Balance full scale load and uncertainty.

Rotor Balance			
Component	Full scale load	Accuracy of Load	Accuracy of Coefficient
Thrust	± 400 lbf	± .56 lbf	± 0.000014
Axial force	50 lbf	± .135 lbf	± 0.000003
Side force	± 50 lbf	± .105 lbf	± 0.000020
Pitching moment	± 1473.8 in-lbf	± 2.35 in- lbf	± 0.000019
Rolling moment	± 1473.8 in-lbf	± 2.21 in- lbf	± 0.000023
Yawing moment	± 1801.2 in-lbf	± .075 in-lbf	± 0.000003
Body Balance			
Component	Full scale load	Accuracy	Accuracy of Coefficient
Normal force	± 1200 lbf	± 1.32 lbf	± 0.0015
Axial force	125 lbf	± .188 lbf	± 0.0001
Pitching moment	± 2000 in-lbf	± 3 in-lbf	± 0.0015
Rolling moment	± 1000 in-lbf	± 1.1 in-lbf	± 0.0005
Yawing moment	± 2000 in-lbf	± 1.4 in-lbf	± 0.0007
Side force	± 500 lbf	± .45 lbf	± 0.0005

Table 3. Test Conditions

Data Set	Data Range	Hex	Tri
Trim Sweep	$40 \rightarrow 140$ KTAS ($\alpha = 0 \rightarrow -5.5, \beta = 0$)	X	X
Alpha Sweep	$0 \rightarrow -9$ deg @ 100 KTAS ($\beta = 0$)	X	X
Beta Sweep	$-16 \rightarrow 16$ @ 100 KTAS ($\alpha = 0$)	X	X
Speed Sweep	$40 \rightarrow 140$ KTAS ($\alpha = \beta = 0$)	X	X

Table 4. Configurations Tested

Body + Gun Pod	Hex	Tri	Hex	Tri
Body + Gun + Wing	X	X	X	X
Body + Gun + Wing + 1 Missile	X	X	X	X
Body + Gun + Wing + 2 Missile	X	X	X	X
Body + Gun + Wing ($\alpha = 3$) + 2 Missile	X	X	X	---
Body + Gun + Wing ($\alpha = 6$) + 2 Missile	X	X	X	---

Test Section Ceiling

Drive Shaft

83.13
Center of Hub

84.02
Center of
Shaft Tilt

87.00

Rotor Balance

Tunnel C_L,
Center of
FuselageTilt

Test Section Floor
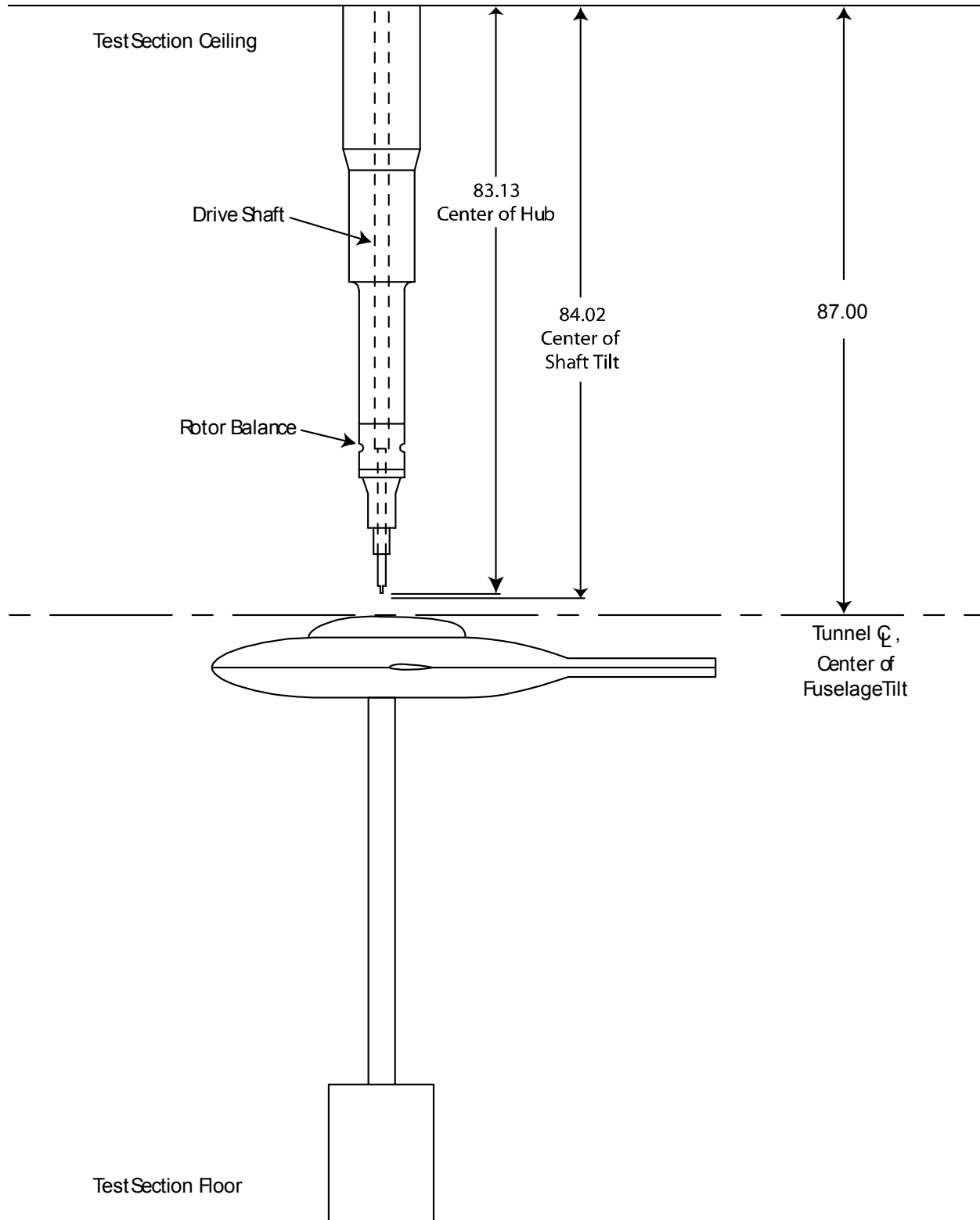
Figure 1. Sketch of the side view of the Isolated Rotor Test System and model arrangement. (All dimensions in inches.)

1. Select Cross Section
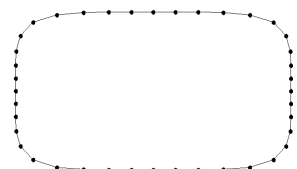
3. Select Shape Function
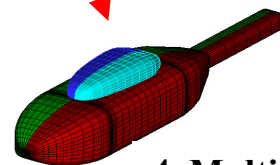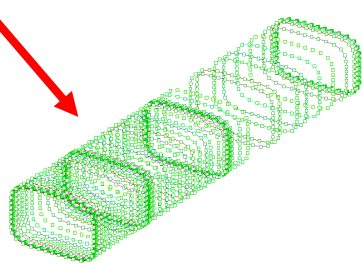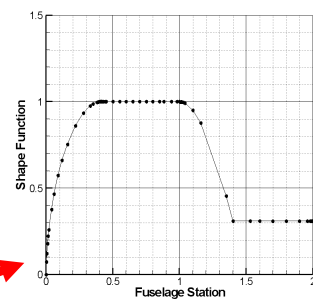
2. Form Body Cylinder

4. Multiply Cylinder by Shape Function to Produce Model

Figure 2. Model design process.
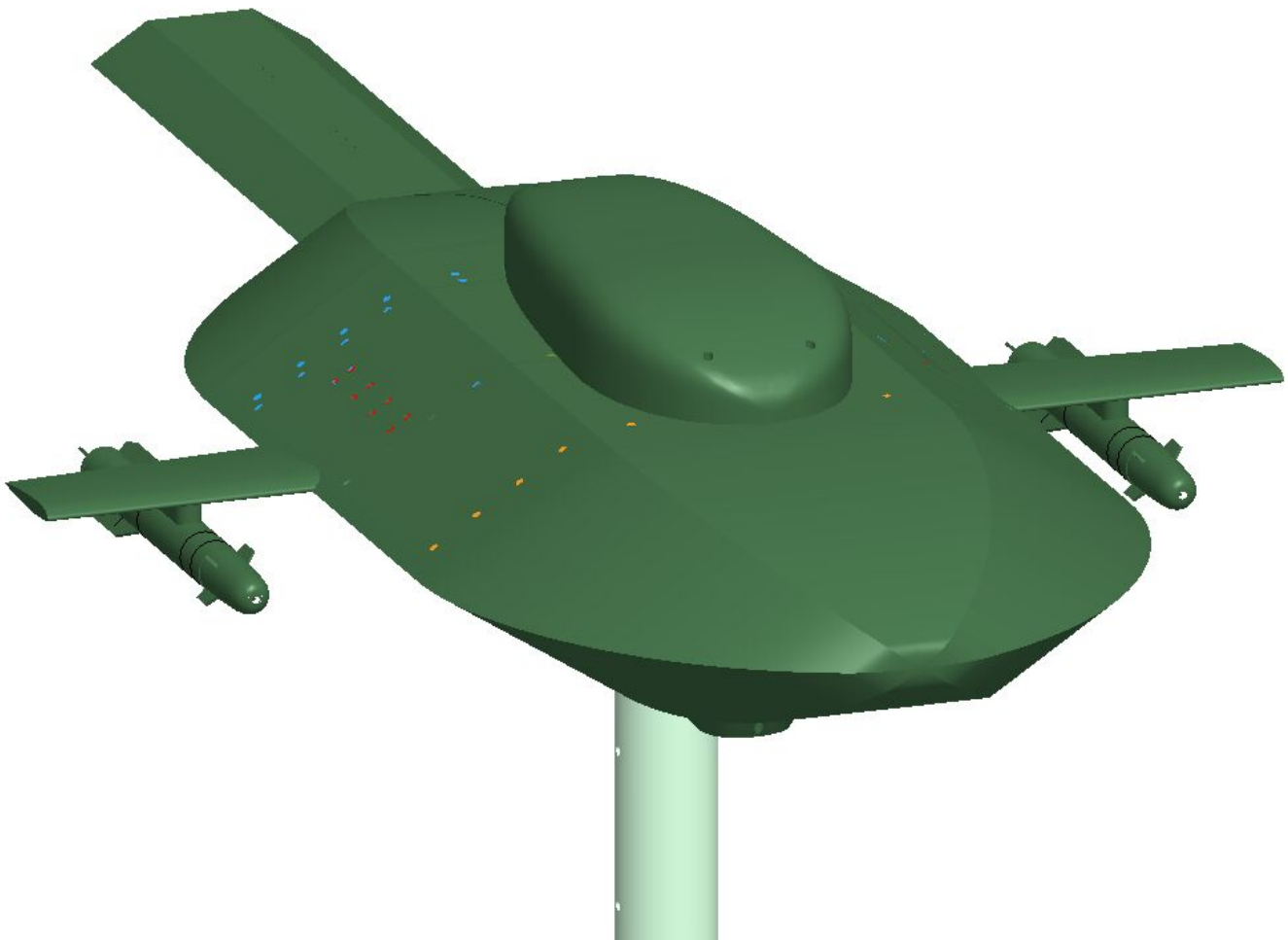
Figure 3 Hex model configuration.
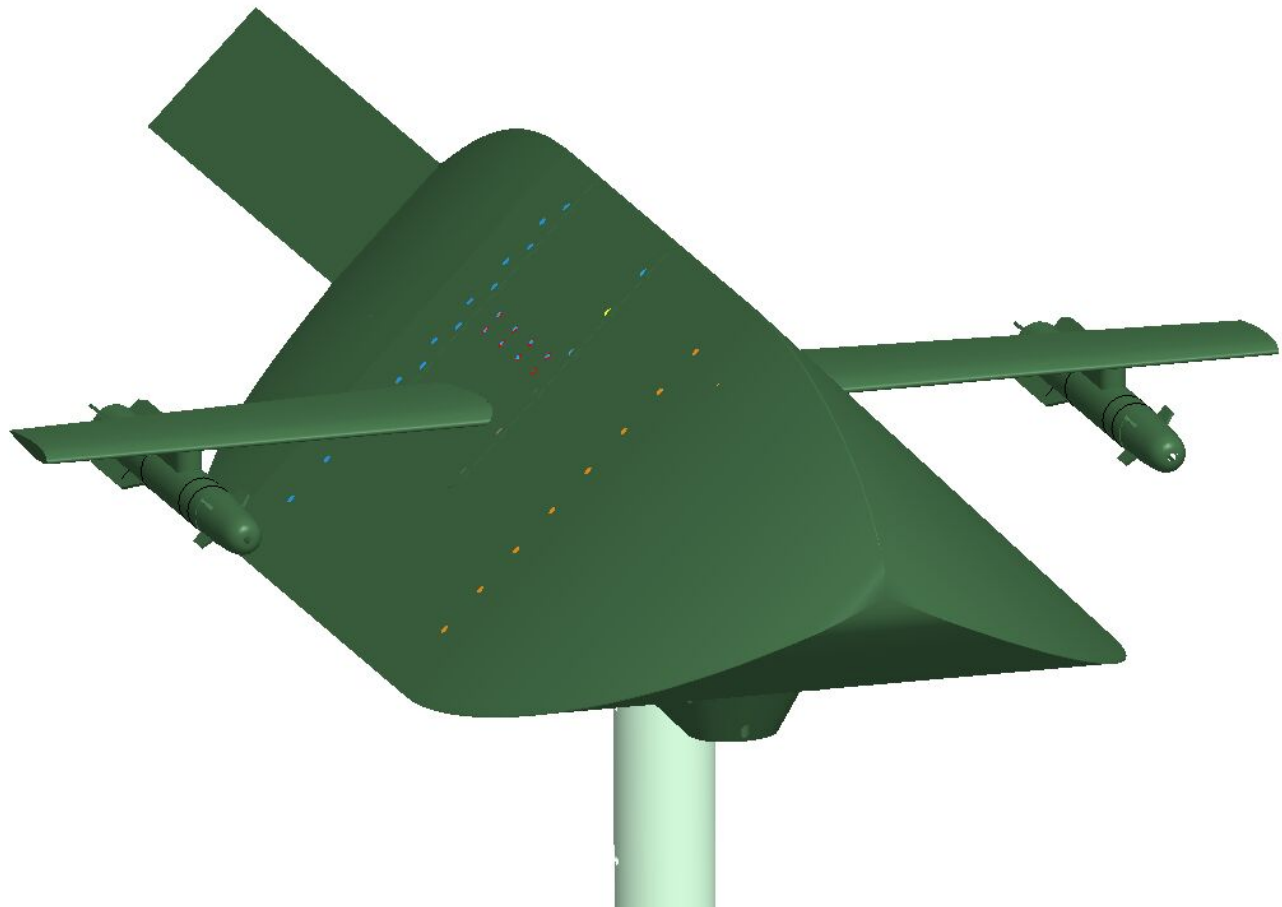
Figure 4 Tri model configuration
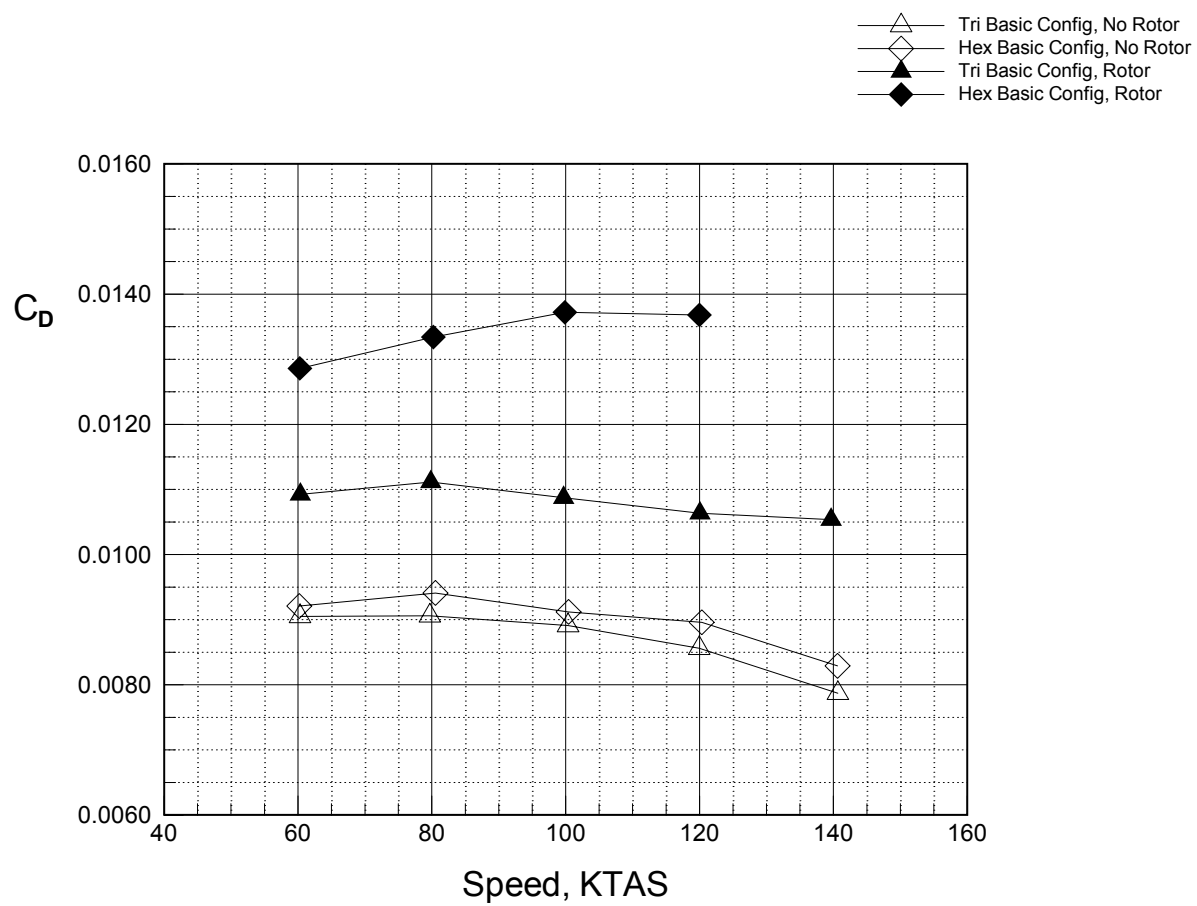
Figure 5. Variation of drag coefficient with speed for both basic configurations with and without the rotor, $\alpha = \beta = 0^0$.
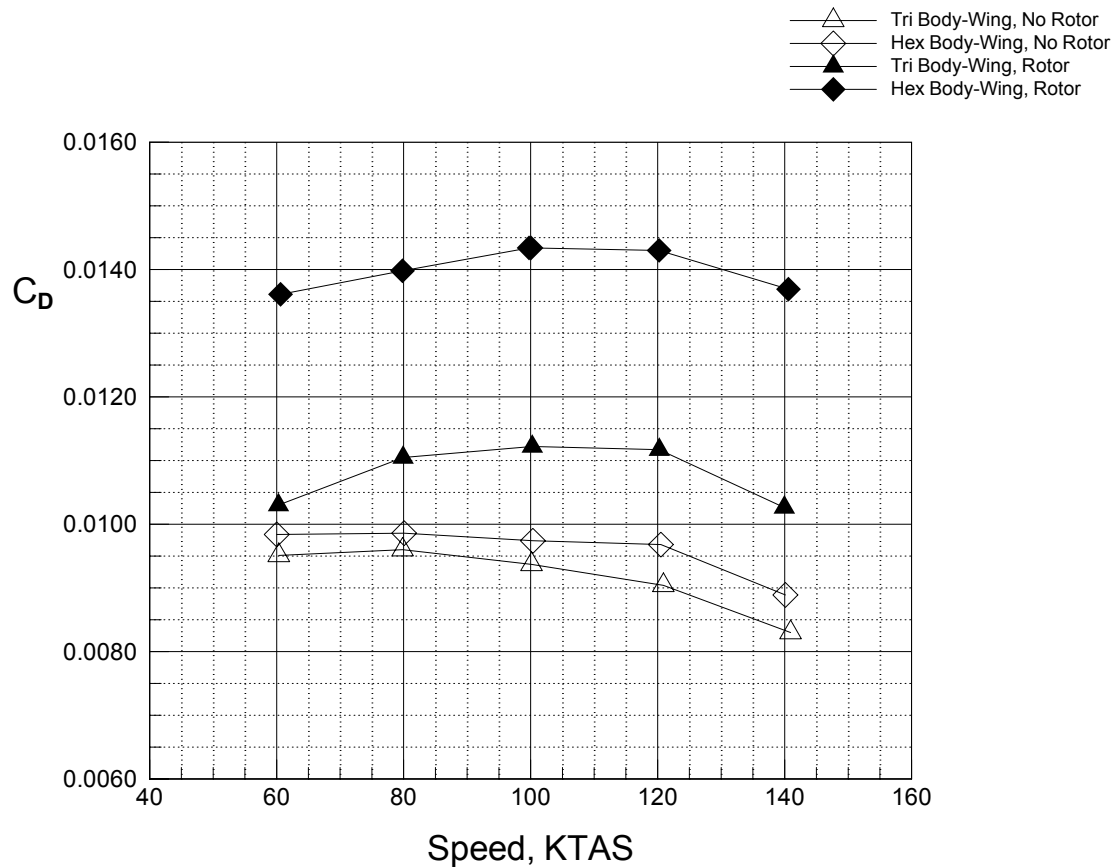
Figure 6. Variation of drag coefficient with speed for both basic configurations plus the wing, with and without the rotor, $\alpha = \beta = 0^0$.
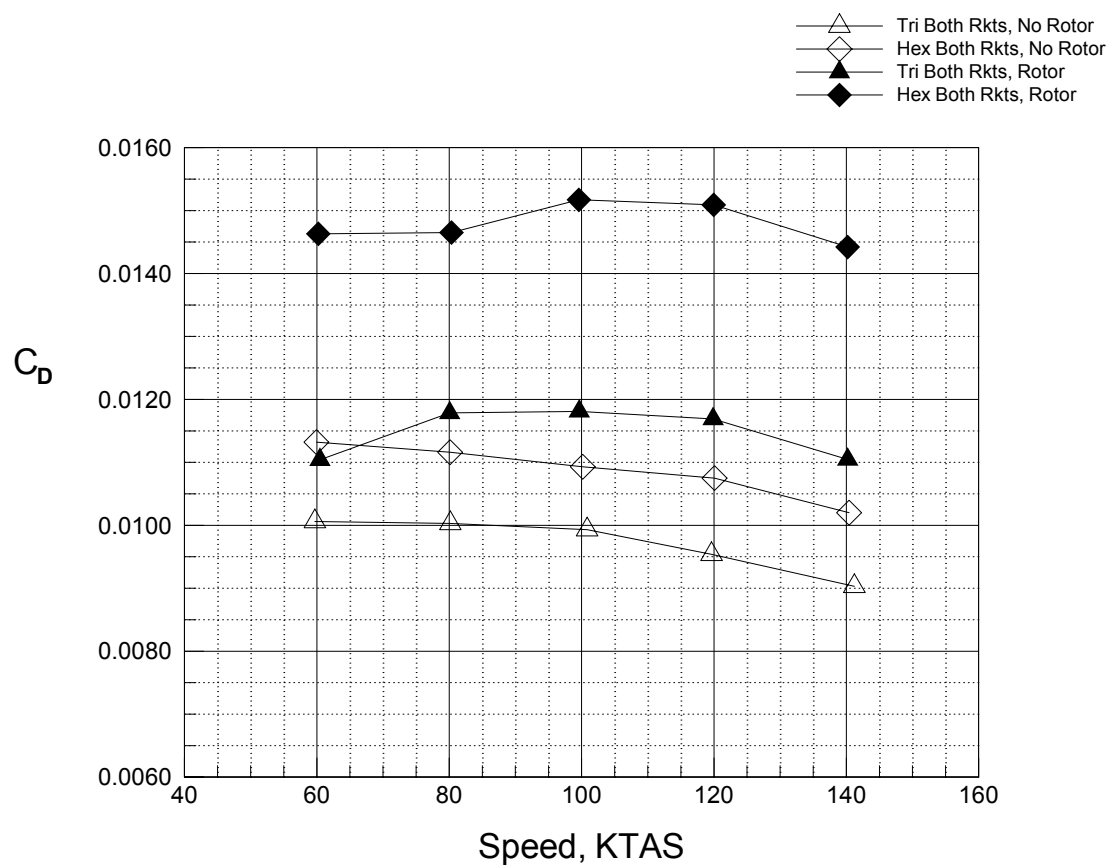
Figure 7. Variation of drag coefficient with speed for both basic configurations plus the wing and rockets, with and without the rotor, $\alpha = \beta = 0^0$.
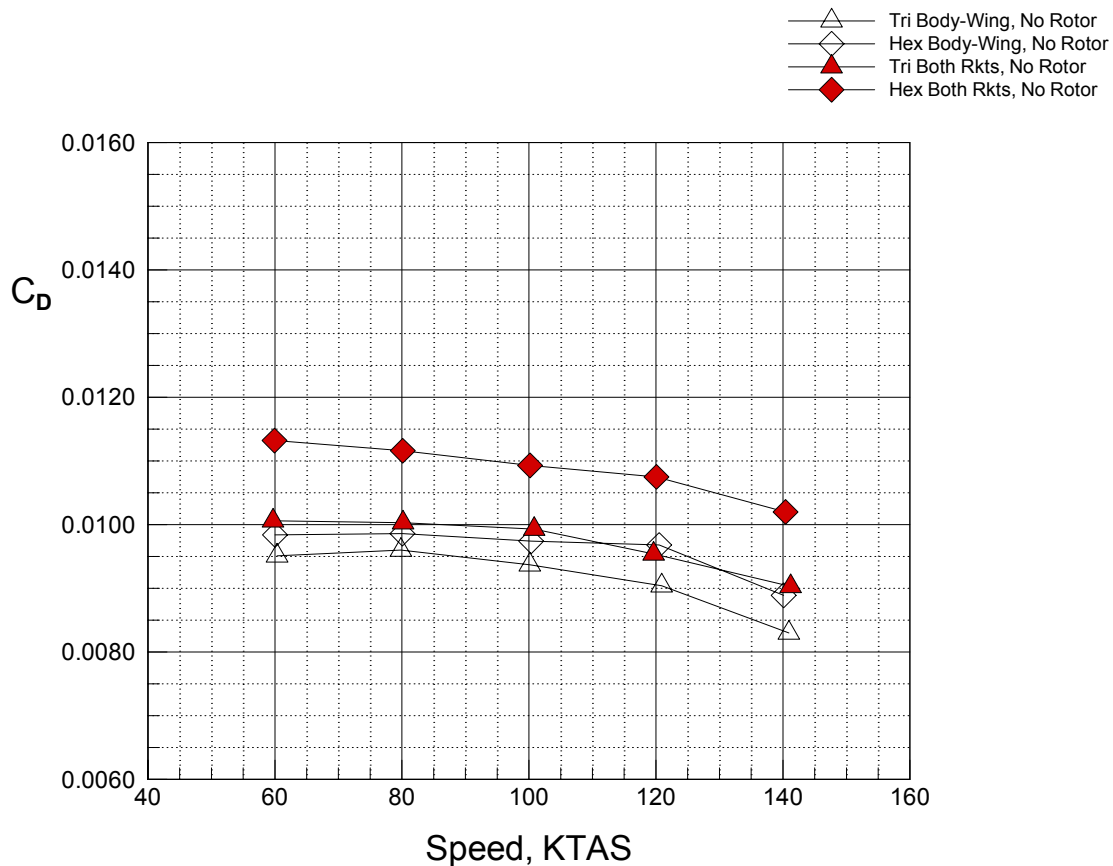
Figure 8. Variation of drag coefficient with speed for both basic configurations plus the wing, without the rockets and no rotor $\alpha = \beta = 0^0$.
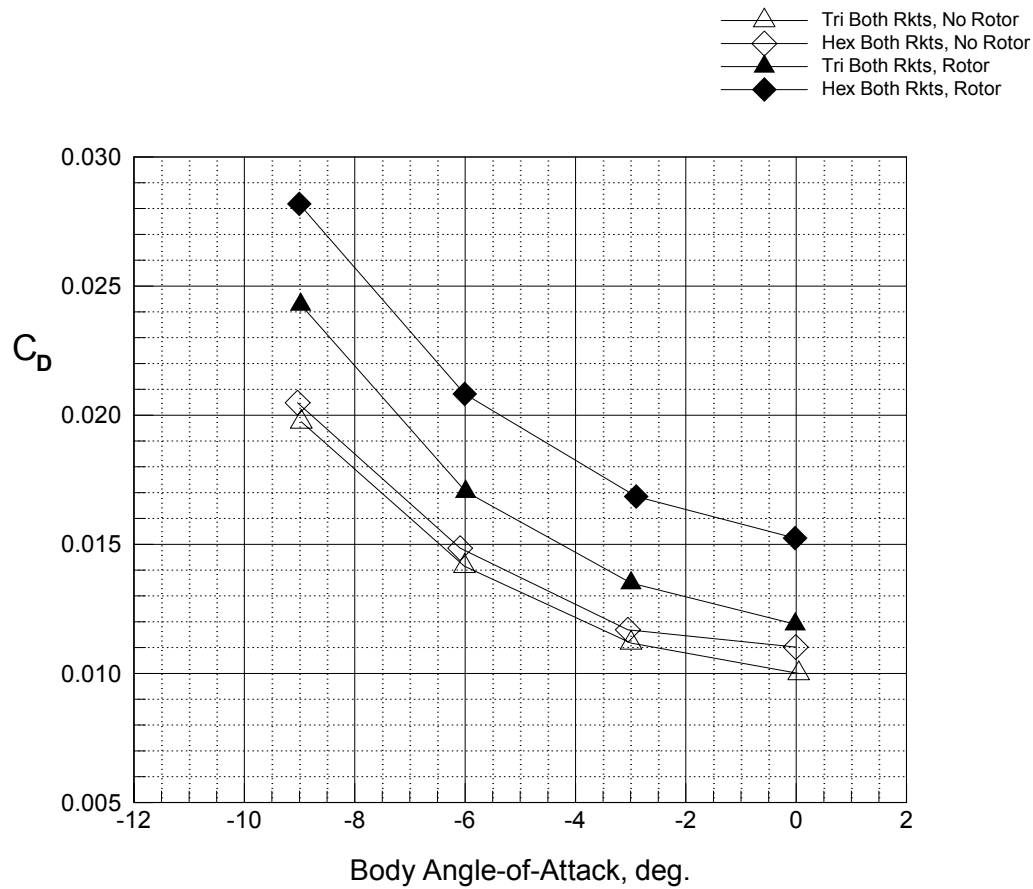
Figure 9. Variation of drag coefficient with angle-of-attack for both basic configurations plus the wing, and rockets with and without the rotor, $\beta = 0^0$, V = 100 knots.
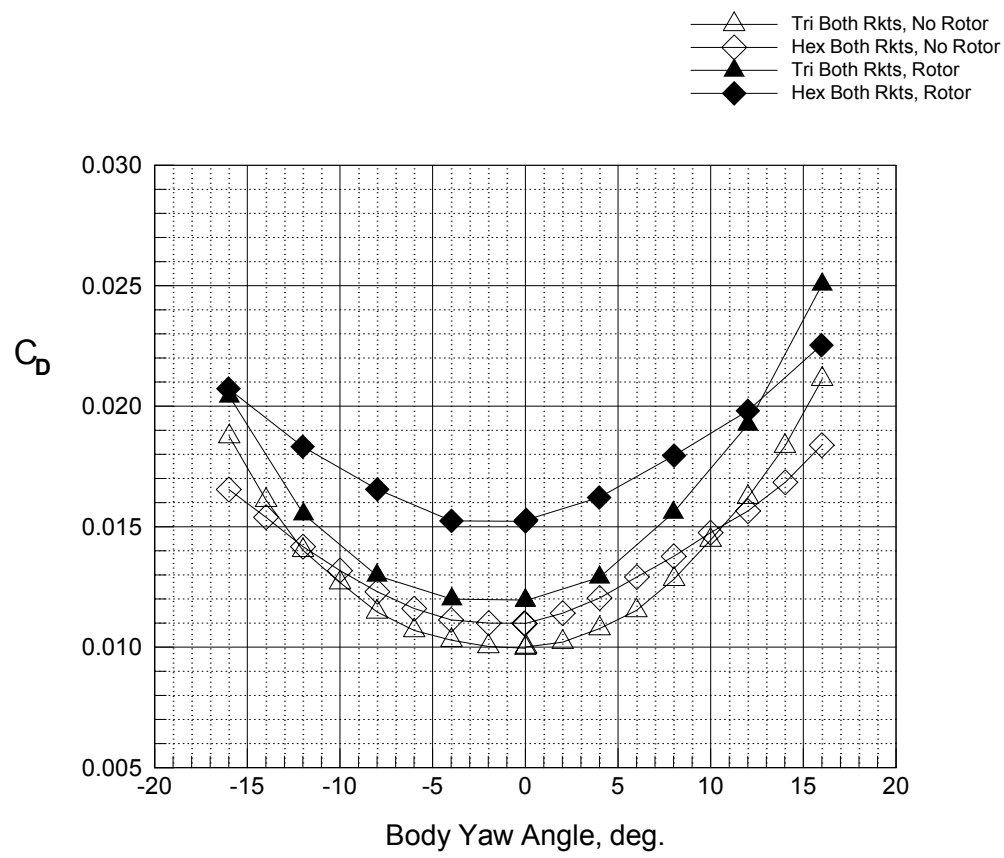
Figure 10. Variation of drag coefficient with yaw angle for both basic configurations plus the wing, and rockets with and without the rotor, $\alpha = 0^0$, V = 100 knots.
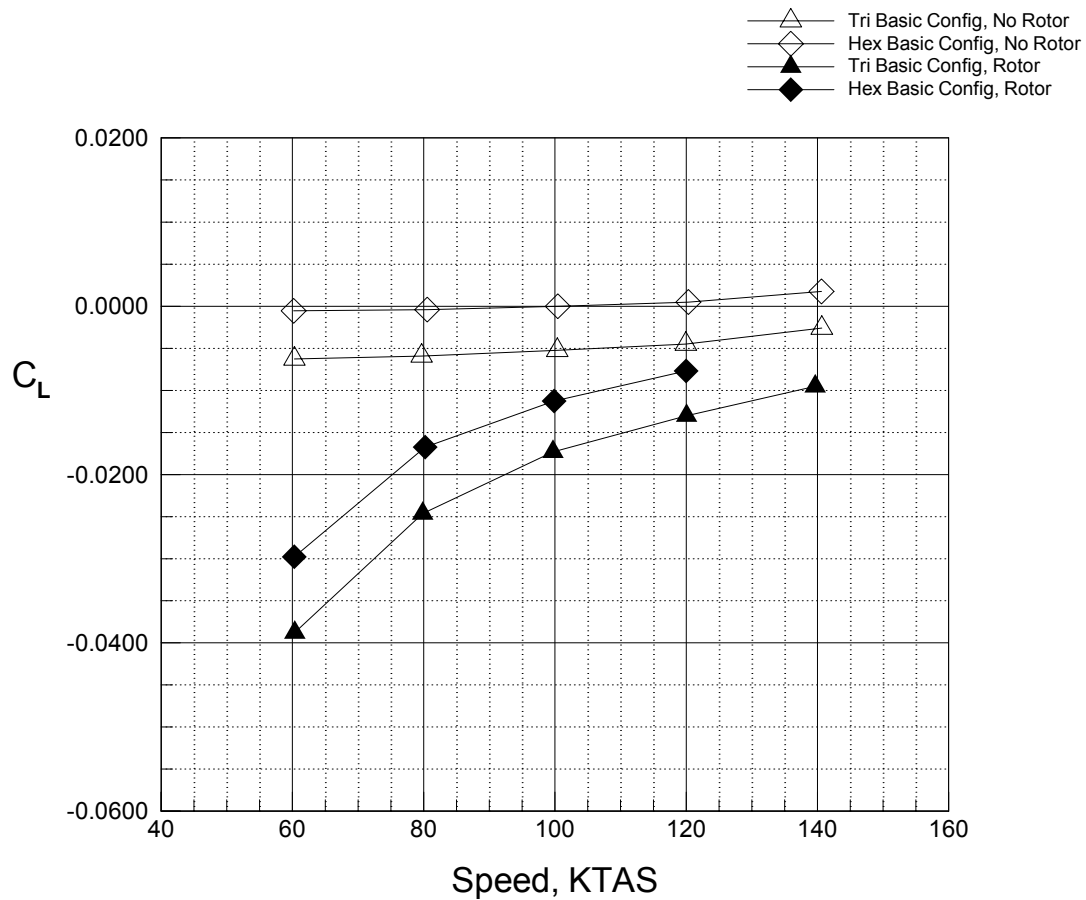
Figure 11. Variation of lift coefficient with speed for both basic configurations with and without the rotor, $\alpha = \beta = 0^0$.
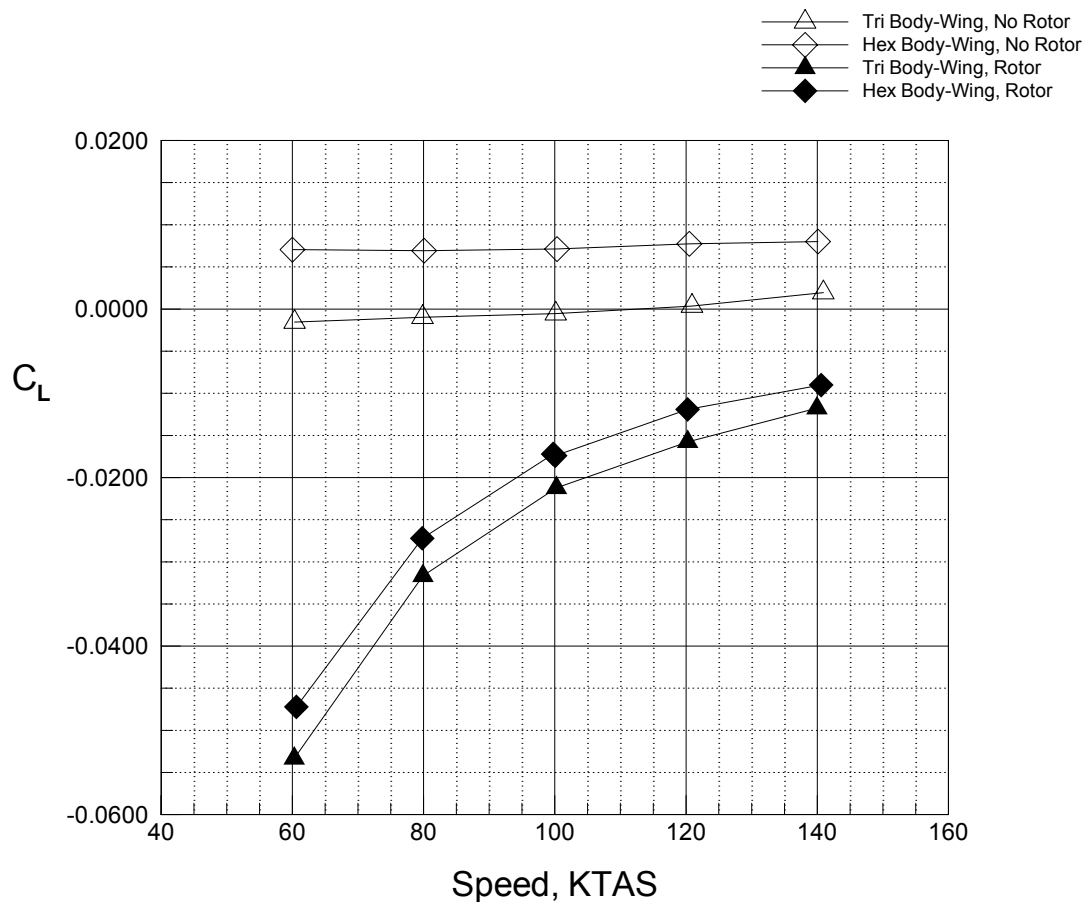
Figure 12. Variation of lift coefficient with speed for both basic configurations plus the wing, with and without the rotor, $\alpha = \beta = 0^0$.
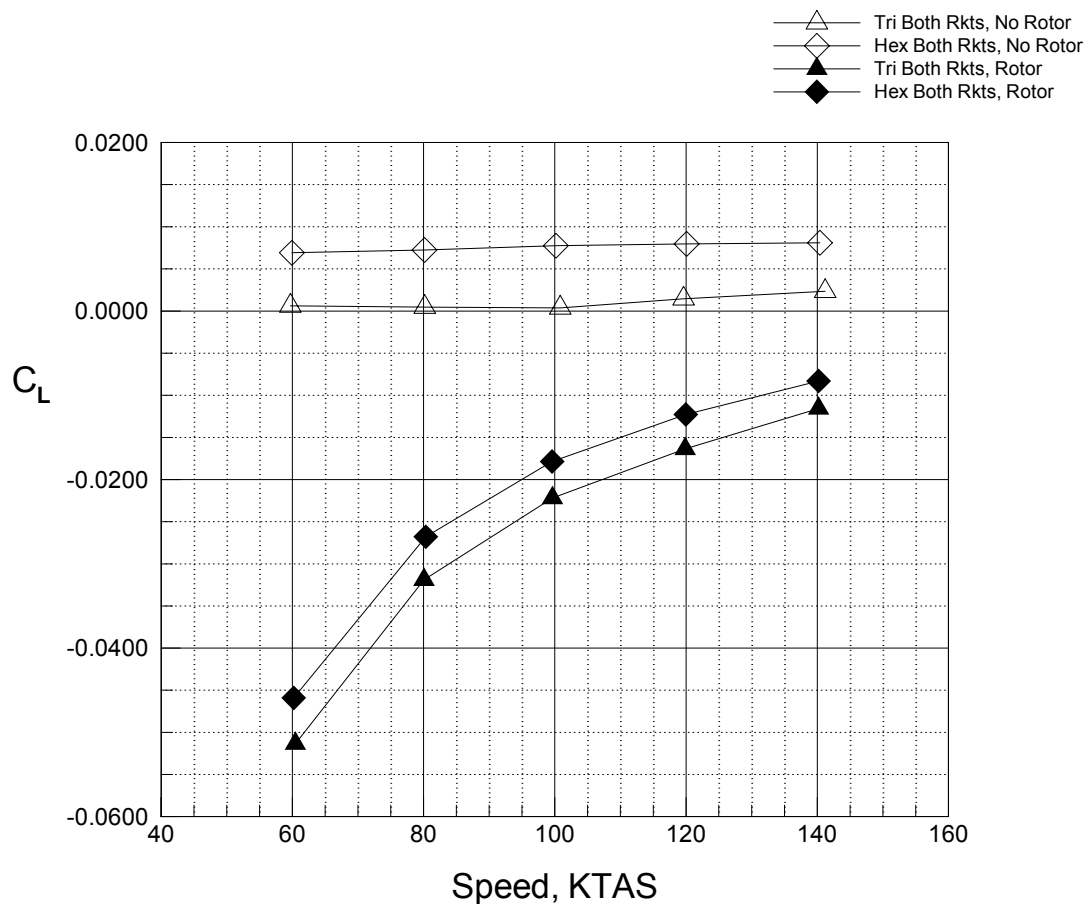
Figure 13. Variation of lift coefficient with speed for both basic configurations plus the wing and rockets, with and without the rotor, $\alpha = \beta = 0^0$.
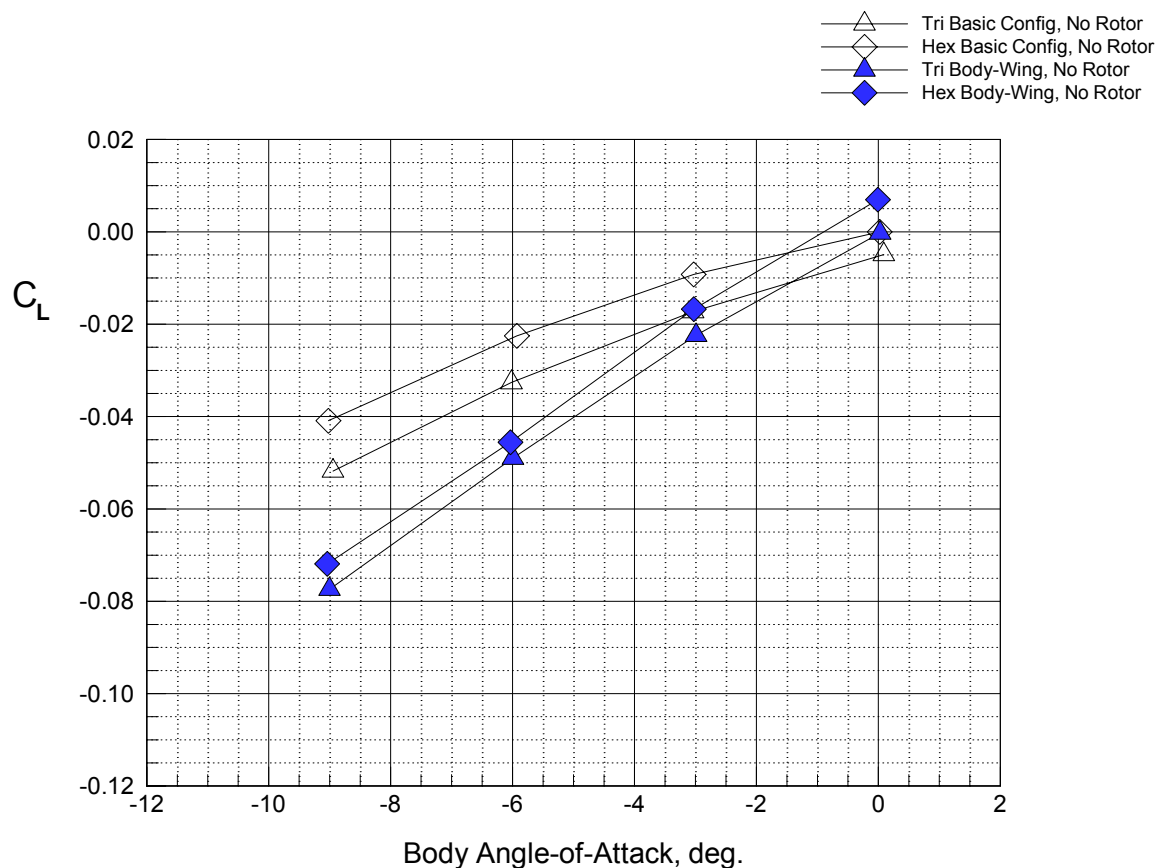
Figure 14. Variation of lift coefficient with angle-of-attack for both basic configurations with and without the wing and no rotor, $\beta = 0^0$, V = 100 knots.
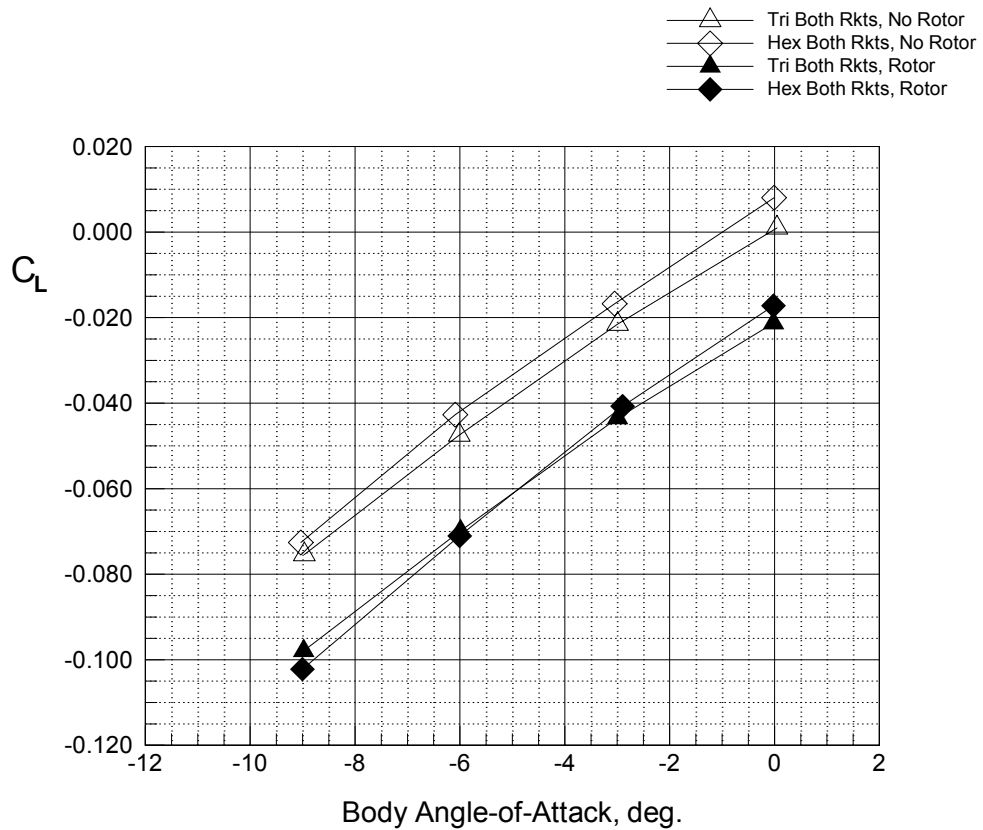
Figure 15. Variation of lift coefficient with angle-of-attack for both basic configurations plus the wing, and rockets with and without the rotor, $\beta = 0^0$, V = 100 knots
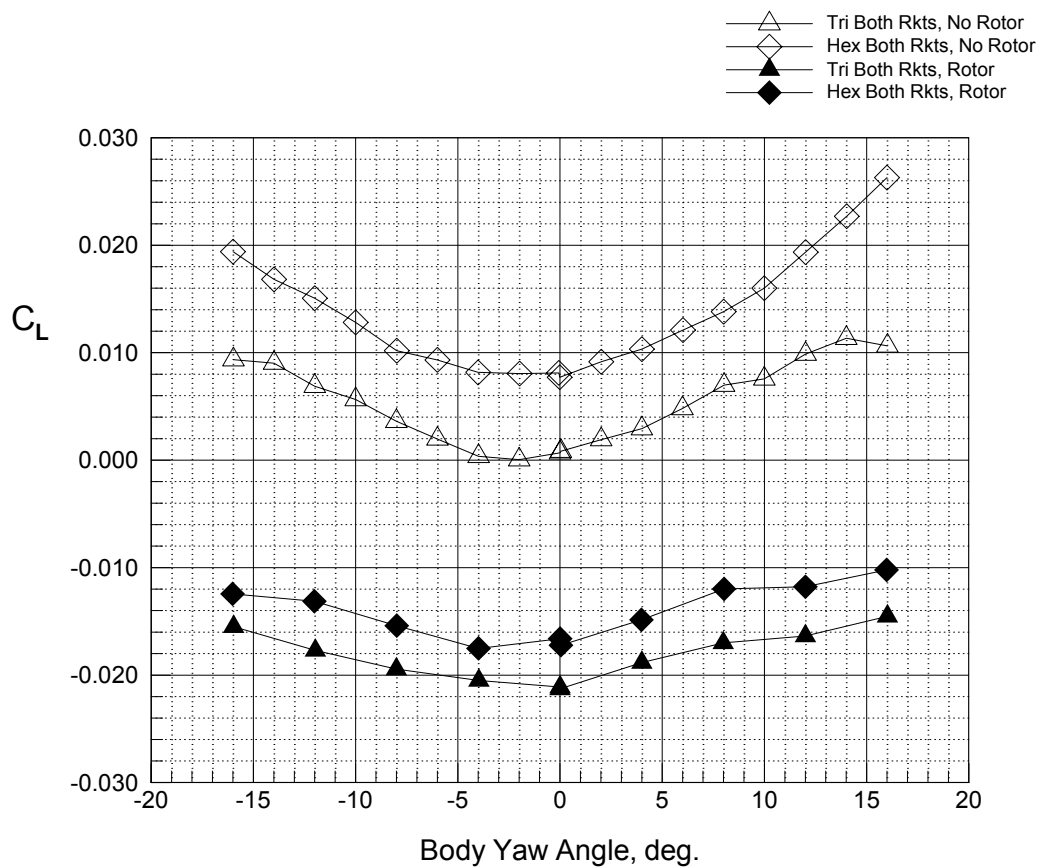
Figure 16. Variation of lift coefficient with yaw angle for both basic configurations plus the wing, and rockets with and without the rotor, $\alpha = 0^0$, V = 100 knots.